Journal of Materials Chemistry A

ROYAL SOCIETY OF CHEMISTRY

PAPER

View Article Online
View Journal | View Issue

Cite this: J. Mater. Chem. A, 2023, 11, 5670

Towards economic processing of high performance garnets – case study on zero Li excess Ga-substituted LLZO†

Christian Schwab, [a] Grit Häuschen, [a] Markus Mann, [a] Christoph Roitzheim, [a] Olivier Guillon, [ab] Dina Fattakhova-Rohlfing [ab] and Martin Finsterbusch *[ab]

Received 28th November 2022
Accepted 13th February 2023

DOI: 10.1039/d2ta09250f

rsc.li/materials-a

In this processing study we systematically investigate the impact of lithium excess and dwell time on Ga-substituted LLZO ($Li_{6.4}Ga_{0.2}La_3Zr_2O_{12}$). To draw a holistic picture of the underlying dependencies for maximum performance, we study the composition, phase formation, density and microstructure, especially with respect to the grain boundaries, in detail. For the first time, we show that Li-excess during synthesis and processing is not just unnecessary for LLZO:Ga, but that high amounts of Li excess can also prevent obtaining peak performance or increase energy and precursor consumption to a non-feasible level for industrial application. We show that the underlying mechanism is an intricate interplay between phase equilibria of different phases (tetragonal, cubic, Li–La–Ga), which have good conductivity and/or act as sintering aids (in low amounts) but are detrimental to electrochemical performance in large amounts. Based on this understanding, we developed a reproducible and robust processing route for LLZO:Ga, minimizing Li excess and dwell time while maintaining high conductivity in the final component. This can make the LLZO family more viable for application in high energy density all-solid-state batteries and provide a pathway for economic industrial processing.

Introduction

The garnet-type solid lithium-ion conductor $Li_7La_3Zr_2O_{12}$ (LLZO) is being intensively investigated as one of the most promising oxide electrolytes for solid-state batteries. LLZO is an electronic insulator, chemically stable against lithium metal, which enables the use of lithium metal anodes and has a good Li-ion conductivity of up to 1 mS cm^{-1} at room temperature. To achieve these conductivities, dopants and substituents are required to stabilize the cubic LLZO structure and increase the number of lithium vacancies.[1–5] Al, Ga, Ta and Nb are typical substituents. Trivalent substituents, such as Al and Ga ions, occupy the lithium position ($Al_{Li}^{\cdot\cdot}$, $Ga_{Li}^{\cdot\cdot}$), while higher-valent Ta and Nb ions are incorporated into the Zr sub-lattice ($Ta_{Zr}^{\cdot\cdot}$, $Nb_{Zr}^{\cdot\cdot}$). Another approach of substituting La sites by larger but lower-valent Rb ions to broaden the Li diffusion path also proved successful in increasing overall conductivity despite lowering the amount of Li vacancies.[6]

Unintentional substitution with Al is often due to uptake from alumina crucibles during synthesis and is difficult to avoid in large-scale commercial synthesis. However, substitution with Al stabilizes the cubic phase and increases the total Li-ion conductivity by three orders of magnitude to low 10^{-4} mS cm^{-1} at room temperature (RT) compared to unsubstituted tetragonal LLZO.[7–11] Substitution with Nb or Ta shows higher conductivity than Al, typically in the mid 10^{-4} mS cm^{-1} range, but niobium leads to instabilities with Li, limiting its application in batteries.[12]

Recently, the substitution with Ga (LLZO:Ga) has attracted a lot of attention, as several studies report total Li-ion conductivities at RT exceeding 1 mS cm^{-1},[7–11] which is a threshold value for high performance mixed cathodes.[13] In addition to increased conductivity, it was also shown that the addition of Ga lowers the energy barrier between the tetragonal and octahedral lithium positions, leading to a lower activation energy of lithium diffusion.[7–11] In comparison to Ta substituted LLZO the crystal structure changes from cubic $Ia\bar{3}d$ (no. 230) to cubic $I\bar{4}3d$ (no. 220) at a degree of substitution of 0.07 per formula unit. In the latter structure, an additional diffusion path is present that further reduces the activation energy of lithium diffusion.[7,14] Table 1 lists the structural and electrochemical parameters of unsubstituted tetragonal and cubic Ta- and Ga-substituted LLZO, illustrating the relationships above.

Table 2 summarizes several studies of LLZO:Ga samples with different Li excess of 10% and 20%, with dwell times and

[a]Institute of Energy and Climate Research, Materials Synthesis and Processing (IEK-1), Forschungszentrum Jülich GmbH, Wilhelm-Johnen-Straße, 52425 Jülich, Germany. E-mail: m.finsterbusch@fz-juelich.de

[b]Helmholtz Institute Münster: Ionics in Energy Storage (IEK-12), Forschungszentrum Jülich GmbH, Corrensstr. 46, 48149 Münster, Germany

† Electronic supplementary information (ESI) available. See DOI: https://doi.org/10.1039/d2ta09250f

Table 1 Comparison of structural and electrochemical parameters of different LLZO phases and substituents

	Tetragonal LLZO	Cubic LLZO:Ta	Cubic LLZO:Ga
Composition	$Li_7La_3Zr_2O_{12}$	$Li_{6.2}Al_{0.2}La_3Zr_{1.8}Ta_{0.2}O_{12}$	$Li_{6.4}Ga_{0.2}La_3Zr_2O_{12}$
M (g mol^{-1})	839.73	857.52	849.51
Space group	$I4_1/acd$ (no. 142)	$Ia\bar{3}d$ (no. 230)	$I\bar{4}3d$ (no. 220)
a (Å)	13.1200(7)	12.958(1)	12.9936(2)
c (Å)	12.6753(7)	$=a$	$=a$
ρ (g cm^{-3})	5.11	5.24	5.144
σ (S cm^{-1})	2.58×10^{-5}	6.14×10^{-4}	1.32×10^{-3}
E_a (eV)	0.46	0.29	0.256
Ref.	15	16	9

Table 2 Literature comparison of electrochemical performance dependent on the sintering program

Nominal composition	Rel. density (%)	Li excess (mol%)	Sintering conditions	σ_{total} (mS cm^{-1})	T_σ (°C)	E_a (eV)	Ref.
$Li_{6.45}Ga_{0.05}La_3Zr_{1.6}Ta_{0.4}O_{12}$		20	30 h, 1175 °C	0.75	30	0.34	8
$Li_6Ga_{0.15}La_3Zr_{1.75}Ta_{0.25}O_{12}$	91	10	4 h, 1100 °C	0.67	25	0.33	18
$Li_{6.55}Ga_{0.15}La_3Zr_2O_{12}$		10	6 h, 1230 °C	0.88	20	0.26	9
$Li_{6.55}Ga_{0.15}La_3Zr_2O_{12}$		10	12 h, 1075 °C	2.06	25	0.246	19
$Li_{6.55}Ga_{0.15}La_3Zr_2O_{12}$		10	12 h, 1050 °C	0.89	25	0.258	19
$Li_{6.55}Ga_{0.15}La_3Zr_2O_{12}$		10	12 h, 1100 °C	0.36	25	0.293	19
$Li_{6.55}Ga_{0.15}La_3Zr_2O_{12}$	~94	10	6 h, 1085 °C	1.3	24	0.3	10
$Li_{6.4}Ga_{0.2}La_3Zr_2O_{12}$		20	30 h, 1175 °C	1.48	30	0.27	8
$Li_{6.4}Ga_{0.2}La_3Zr_2O_{12}$		10	6 h, 1230 °C	1.32	20	0.256	9
$Li_{6.4}Ga_{0.2}La_3Zr_2O_{12}$	~94	20	18 h, 1200 °C	1.09	RT	0.22	11
$Li_{6.4}Ga_{0.2}La_3Zr_2O_{12}$	~94	10	6 h, 1085 °C	0.9	24	—	10
$Li_{6.35}Ga_{0.15}Nb_{0.2}La_3Zr_{1.8}O_{12}$	~95	10	6 h, 1150 °C	0.73	30	0.34	20
$Li_{6.25}Ga_{0.25}La_3Zr_2O_{12}$	94.1	10	24 h, 1100 °C	1.46	25	0.25	21
$Li_4Ga_{1.0}La_3Zr_2O_{12}$	92.5	20	6 h, 1085 °C	0.54	20	0.32	22
$Li_{6.25}Ga_{0.25}La_3Zr_2O_{12}$	98.8	10	1 h, 1100 °C, hot pressed	1.24	25	0.2	23

temperatures varying from 6 h to 30 h and 1050 °C to 1230 °C, respectively. It should be noted, that at Ga levels higher than 0.05, which are necessary to foster the high total conductivity, LLZO:Ga seems to be unstable in combination with Li metal. Nevertheless, no clear dependence of the electrochemical performance on the processing parameters can be deducted from the table. However, a clear understanding of the relationship between processing parameters and -performance is necessary for industrial scale production as it affects efficiency and resource and energy cost. Only for Al substituted LLZO there are studies investigating the parameter–performance relationship,[17] but no such studies exist yet for the highly conductive LLZO:Ga. To fill this knowledge gap, we comprehensively investigate gallium-substituted LLZO with $Li_{6.4}Ga_{0.2}La_3Zr_2O_{12}$ composition to determine the optimal sintering conditions for maximum performance. We synthesized LLZO:Ga with different amounts of lithium excess (0–20%) and different dwell times (1–20 h). The samples were characterized by X-Ray Diffraction (XRD), Particle Size Distribution (PSD), Inductively Coupled Plasma – Optical Emission Spectroscopy (ICP-OES), Scanning Electron Microscopy (SEM), Energy-dispersive X-ray Spectroscopy (EDX), Time-of-Flight-Secondary Ion Mass Spectrometry (ToF-SIMS) and Electrochemical Impedance Spectroscopy (EIS) during the various synthesis and processing steps, providing valuable insight into the processing-induced changes in material properties and the resulting impact on final electrochemical performance.

Experimental

The garnet LLZO:Ga powders were synthesized *via* a classic three step solid state reaction. The starting materials $LiOH \cdot H_2O$ (AppliChem GmbH, 99%), La_2O_3 (Merck Chemicals GmbH, 99.9%, 10 h pre-dried at 900 °C), ZrO_2 (Treibacher Industrie AG, 99.7%) and Ga_2O_3 (Alfa Aesar, 99.995%) were weighed in stoichiometric amounts. Excess $LiOH \cdot H_2O$ was varied between 0–20% to counteract lithium loss during sintering.

The weighed in powder was mixed for 5 min, ground for 1 h and afterwards mixed again. Pellets were pressed from the homogenized powder (uniaxial, 20 MPa) and calcined twice for 20 h in alumina crucibles.

The first calcination step was performed at 850 °C, whilst the second one at a higher temperature of 1000 °C. After each calcination step the pellets were ground and repressed. The final pellets were uniaxial pressed at 113 MPa. To avoid possible contamination, the pellets were sintered in mother powder of the same composition in closed alumina crucibles at 1175 °C for 1–20 h in air. Heating and cooling ramps for calcination and sintering steps of 5 K min^{-1} were chosen.

X-ray diffraction (XRD) measurements were performed to check phase purity and structure of the samples. All measurements were recorded on a Bruker D4 Endeavour instrument using Cu-K_α-radiation and equipped with a 1D detector LYNXEY and a DIFFRAC^{plus} BASIC package, which was released in 2009. All samples were measured from 10 to 80° 2Θ and a step size of 0.02°. For the measurements the pellets were crushed and mortared to fine powder to ensure good statistics. Rietveld refinement was performed using the Fullprof program package[24] and the least squared method. The peak shape was described by a pseudo-Voigt function and the background level was defined by a polynomial function with six refinable coefficients. Scale factor, zero point correction, asymmetry parameters, and the lattice parameter a were refined in addition to the atom positions. The reported crystal structure of $Li_{6.49}Ga_{0.20}La_{2.94}Zr_2O_{12}$ (ref. 7) was used as starting crystal structure model. The estimated standard deviation of the lattice parameter $\sigma(a)$ has been obtained by multiplying it by the SCOR parameter (Berar's factor) given by the FULLPROF program.[25]

The particle size distributions of the calcined powders were determined by laser light scattering on a Horiba LA-950V2 Laser Particle Size Analyzer (Retsch GmbH).

The density was measured geometrically. The relative density was calculated as the ratio of geometrically determined density and crystallographic density determined by Rietveld refinements.

Inductively Coupled Plasma - Optical Emission Spectroscopy (ICP-OES; Thermo Elemental, IRIS Intrepid iCAP 7600) was used for stoichiometry determination of the calcined and sintered LLZO:Ga samples. Therefore, 50 mg of the respective powders were dissolved in 4 mL sulfuric acid. 2 g of ammonium sulfate were added under strong heating. The solutions were filled up to 50 mL and diluted to a factor of 1/10 and 1/200 of the concentration. Each measurement was repeated three times.

A cross-section was cut from the pellets and subsequently embedded in epoxy resin. The embedded pellet was polished to a 4000 grit SiC sandpaper finish and polished for additional 30 min using a 1 μm diamond suspension. A thin platinum layer was sputtered onto the sample surface to compensate charging effects.

SEM images were taken on a ZEISS Gemini 450 equipped with an ULTIMMAX 170 detector from Oxford Instruments and on a ZEISS Ultra 55 equipped with an X-max 80 detector from Oxford Instruments.

Time-of-Fight Secondary Ion Mass Spectrometry (ToF-SIMS) was used to record surface images of selected, polished LLZO:Ga pellets. Mass spectra were taken on a TOF.SIMS 5 NCS system (IONTOF GmbH) equipped with a Bi-Nanoprobe primary ion gun, a Cs-sputter gun and a low-energy electron flood gun for charge compensation. Secondary ions were detected on an Extended Dynamic Range detector. Bi^+ primary ions were used for analysis at an energy of 30 keV. The Cs-sputter gun operated at an energy of 2 keV. Surface images were taken in imaging mode with an analysis raster of 50 μm × 50 μm and a 1024 × 1024 pixel raster in negative polarity after a short period of Cs-pre-sputtering in a 300 μm × 300 μm sputter raster to remove surface contaminants.

To measure the Li-ion conductivity, the prepared LLZO pellets were polished with SiC sandpaper up to 4000 grit to remove possible impurities from the surface. As ion blocking electrodes Gold was sputtered (Cressington 108auto Coater) on both sides of the polished pellets. Electrochemical Impedance spectra were recorded on a Novocontrol Technologies Alpha-A impedance spectrometer in a frequency range of 10 MHz to 1 Hz and a field perturbation of 20 mV mm^{-1}. The temperature dependent impedance was recorded between −40 °C and +60 °C in a temperature-controlled chamber (Novocontrol Technologies BDS1100). To fit the equivalent circuits to the measured impedance spectra the program RelaxIS 3 (rhd instruments) was used.

Results and discussion

The objective of this study is to determine the relationship between processing and performance and derive optimized processing parameters for Ga-substituted LLZO ($Li_{6.4}Ga_{0.2}La_3Zr_2O_{12}$) for peak electrochemical performance. To draw a holistic picture of the underlying dependencies for maximum performance, we systematically investigate the effect of Li-excess and dwell times on chemical composition, phase composition, density, and microstructure, especially with respect to grain boundaries. For this purpose, powders and pellets of LLZO:Ga with variable Li-excess were synthesized by a solid state reaction (see Experimental section).

The determined particle size distributions (PSD) of powders containing different amounts of additional Li, ranging from 0% to 20%, after the first and second calcination step are shown in Table 3. While no trend is visible for the lowest 10% (d_{10}) and 50% (d_{50}) PSD fractions after the first calcination step, the highest 10% fraction (d_{90}) shows a systematic increase in grain size with increasing Li excess. After the second calcination step, the d_{10} fraction shows no significant difference compared to the first step, while the d_{50} fraction tends to be smaller after an additional calcination step. This could be due to grain growth of large grains consuming smaller grains. Differences between the first and second calcination step are not evident with respect to increasing Li excess. The d_{90} fraction again exhibits larger grains with increasing Li excess up to a 10%, as expected for

Table 3 Particle size distribution of LLZO:Ga with varying Li excess after the first and second calcination step

Sample	d_{10} (μm)	d_{50} (μm)	d_{90} (μm)
First calcination step			
LLZO:Ga_0%	0.09	3.31	5.87
LLZO:Ga_5%	0.10	4.63	9.69
LLZO:Ga_10%	0.09	4.06	10.77
LLZO:Ga_20%	0.08	3.74	13.25
Second calcination step			
LLZO:Ga_0%	0.08	3.10	9.08
LLZO:Ga_5%	0.13	2.51	11.45
LLZO:Ga_10%	0.13	2.36	12.70
LLZO:Ga_20%	0.08	2.54	8.23

longer combined sintering time and higher temperature. The differences between the first and second calcination are only significant at 20% Li excess, resulting in much smaller grain sizes at the highest substitution level considered.

Rietveld refinement of pure cubic phase LLZO:Ga powder (0% Li excess) shows a second cubic LLZO phase (Fig. 1). While the main phase has a lattice parameter of $a = 12.981(3)$ Å, the second LLZO phase is slightly larger at 13.032(4) Å. This has been observed previously and the second cubic phase could be assigned to protonated LLZO:Ga.[26–28] The protonation of the LLZO sample is due to handling in ambient atmosphere. Since the protonation is reversed during sintering, we assume that the materials are pure. From the lattice parameter of the main phase, we calculated the crystallographic density $\rho = 5.16$ g cm^{-3} of $Li_{6.4}Ga_{0.2}La_3Zr_2O_{12}$, which serves as a reference for the density calculations.

XRD patterns of all four powders (Li excess: 0%, 5%, 10% and 20%) after the second calcination step are shown in Fig. 2. A comparison of the different diffraction patterns shows the cubic structure also for the powder without Li excess. Increasing the amount of excess lithium leads to the formation of a multiphase material consisting of cubic and additional tetragonal LLZO phases. As the excess lithium increases, the proportion of tetragonal secondary phase also increases. Since the tetragonal $Li_7La_3Zr_2O_{12}$ phase contains more lithium than the cubic $Li_{6.4}Ga_{0.2}La_3Zr_2O_{12}$ phase (weigh in stoichiometry), this would explain a driving force toward the tetragonal phase. In addition, a competing Li–La–Ga phase below the XRD detection limit could lead to incomplete Ga-ion incorporation and thus to a cubic phase that is not fully stabilized (*i.e.*, the observed tetragonal phase fraction). However, both processes drive the equilibrium toward tetragonal LLZO, and further analysis at the atomic level would be necessary to clarify the individual contributions. Nevertheless, we can estimate the relationship between the different phases in Fig. 3. Unlike other substituents such as Al or Ta, the excess lithium used during the synthesis of Ga-substituted LLZO can shift the phase equilibrium toward tetragonal LLZO, and additional Li–La–Ga phases may form,

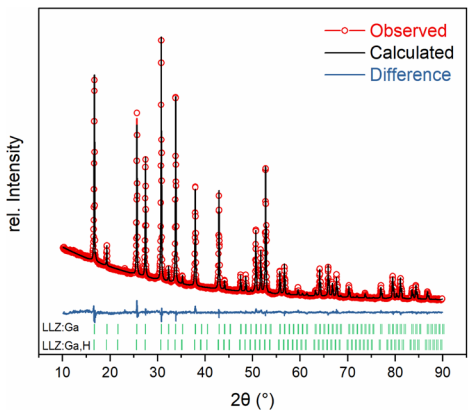

Fig. 1 Rietveld refinement of a $Li_{6.4}Ga_{0.2}La_3Zr_2O_{12}$ powder sample without Li excess. Two cubic phases were identified as pure LLZO (LLZO:Ga) and protonated LLZO (LLZO:Ga,H).

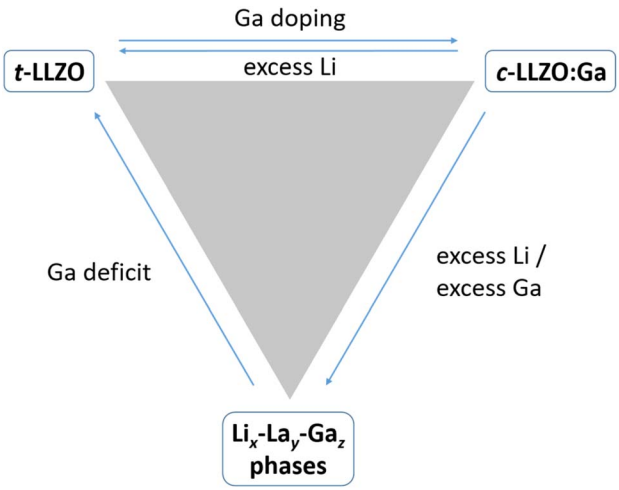

Fig. 3 Relation between tetragonal LLZO, cubic LLZO:Ga and secondary Li–La–Ga phases.

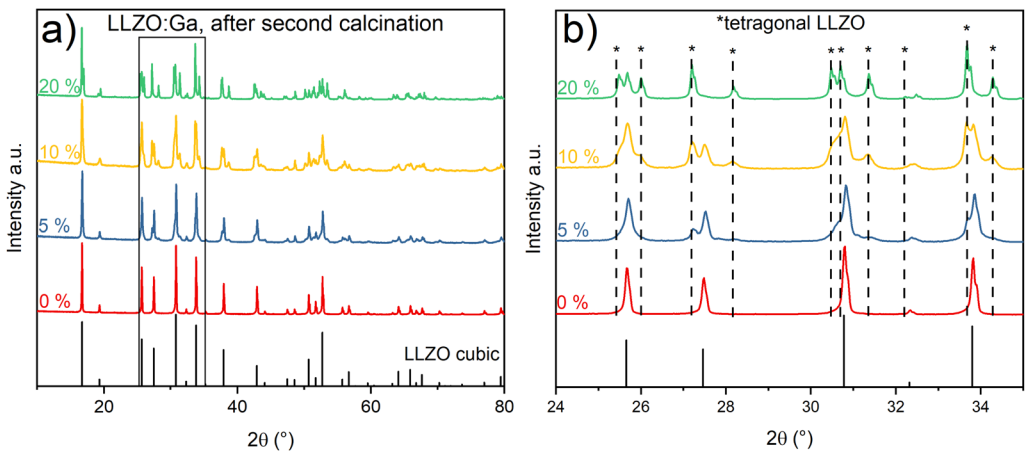

Fig. 2 (a) Powder XRD pattern of LLZO:Ga with different lithium excess content after the second calcination step. (b) Zoomed in region 24–35° 2θ of (a).

leading to a mixture of the three phases. For the desired highly conductive cubic phase the lattice parameter is similar for all Li excess levels and averages 12.978(9) Å.

The lattice parameters of the tetragonal phase are determined to be $a = 13.115(6)$ Å and $c = 12.68(6)$. It is expected to have a lower ionic conductivity and thus poorer electrochemical performance in a battery cell compared to the cubic phase (Table 1). Due to the high vapor pressure of Li, the final high-temperature sintering and associated Li loss can drive the multiphase system into a single phase by effectively lowering the Li excess to zero. However, further heating and loss of lithium can lead to destabilization of the garnet phase and formation of pyrochlore phases, which are non-conductive. Therefore, this interaction is analyzed further in the following sections.

To evaluate the final component performance, calcined powders were pressed into pellets and sintered. Dwell times at a sintering temperature of 1175 °C were varied between 1 h and 20 h and the respective densities measured. Table 4 shows the relative densities of the green and sintered pellets. These range from 90% to 95%, with the highest densities obtained at 5% excess Li. Different amounts of excess lithium do not appear to affect pellet densities at different dwell times. However, for longer dwell times above 10 h, a slight decrease in density is observed in all cases.

After each calcination and sintering step, the chemical composition was determined by ICP-OES. Fig. 4 shows the composition for the different amounts of excess Li. The results were calculated based on a fixed stoichiometry of three La per formula unit. A typical Hf-impurity of 1% in Zr is assumed,[4] and Al impurities were found in all samples at long dwell times caused by alumina crucibles during sintering (see extended Table SI1 in ESI†). Unfortunately, the Zr content in all samples is systematically lower than expected and cannot be readily explained. The contents of lithium and gallium are slightly higher than expected but follow a trend. With the exception of the sample with 0% excess lithium, where similar results are obtained at all dwell times, a trend is observed with increasing dwell times, where the additional amounts of lithium and gallium decrease. Since Li loss at high sintering temperatures is a known phenomenon, a decrease in Li content is expected and is a fundamental part of this study. However, the lithium and gallium contents are higher than the targeted theoretical stoichiometry. Nevertheless, the qualitative trends in this study are consistent with expectations.

For the analysis of X-ray diffraction patterns of the sintered pellets (Fig. SI1a–d in the ESI†), only the unprotonated cubic LLZO:Ga main phase was considered, since the reversibility of the protonation during sintering is well known and the reader is referred to the relevant studies.[26–28] LLZO:Ga pellets without additional Li and at all dwell times retain the cubic crystal structure without any visible secondary phases. At long dwell times of 20 h, the same is observed for 5% Li excess and a phase-pure pellet is obtained. For 10% and 20% Li excess, no phase-pure pellets could be obtained after 20 h. A tetragonal Li-rich $Li_7La_3Zr_2O_{12}$ phase, which was already present in the calcined powder (Fig. 2), is also present even after long dwell times. However, a trend toward decreasing intensity and thus amount of tetragonal phase is observed. This behavior can be explained by two phenomena occurring simultaneously: first, Li loss over time, specifically at very long dwell times, and second, gallium replacing lithium on its lattice site and stabilizing the cubic phase (compare to Fig. 3). In addition, the reduction of the Li excess could lead to destabilization of possible Li–La–Ga secondary phases that might be present. These mechanisms lead to a reduction of the tetragonal phase with increasing dwell time and/or lower Li excess. Fig. 5 compares the diffraction patterns of samples with different Li excess at a dwell time of 5 h and clearly shows an increase in the tetragonal phase with increasing Li excess. This unambiguously confirms the above

Table 4 Relative densities of LLZO:Ga pellets for different dwell times at 1175 °C and different lithium excess

Lithium excess (%)	Green density (%)	1 h (%)	5 h (%)	10 h (%)	20 h (%)
0	64	91.2	97.3	92.7	91.1
5	67	94.5	94.6	92.7	93.4
10	67	93.5	93.5	92.0	91.8
20	66	91.2	91.8	91.5	90.1

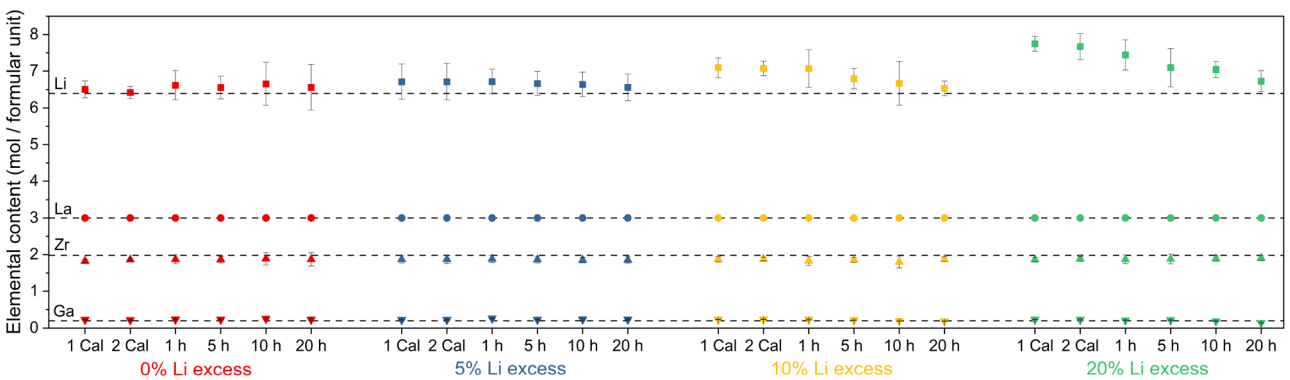

Fig. 4 Comparison of the ICP-OES results for different dwell times and excess lithium. Stoichiometry in reference to La. Theoretical stoichiometry of the ions is indicated by the dotted lines.

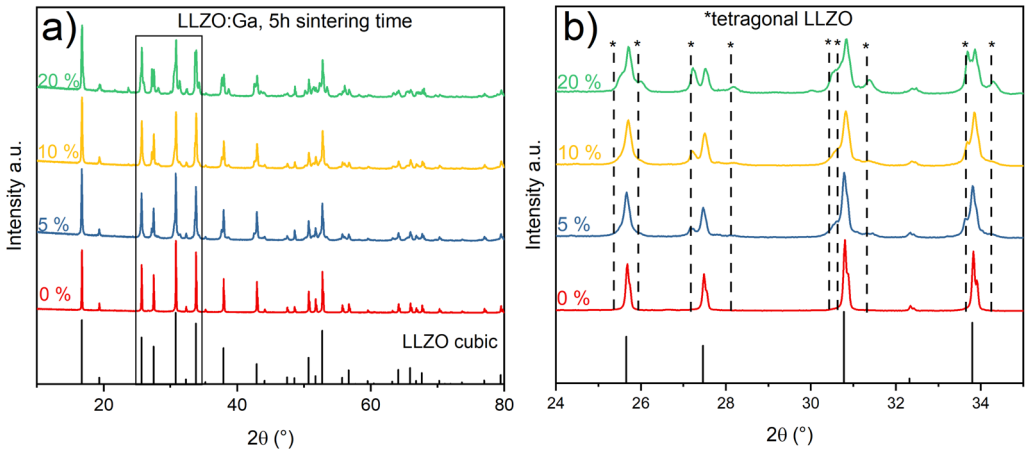

Fig. 5 (a) XRD patterns of samples containing different Li excess at a dwell time of 5 h. An increase of the Li-rich tetragonal LLZO phase with additional lithium is clearly visible. (b) Zoomed in region 24–35° 2θ of (a).

hypothesis of competing phases and shows that process optimization can reduce both precursor excess and dwell time at elevated temperature, leading to a more industrially attractive process.

SEM and EDX analysis of the cross sections of the above samples (Fig. 6) show that without added Li, a homogeneous pellet is obtained with uniformly distributed small pores leading to a closed porosity. A similar microstructure is seen in a pellet with 5% Li excess, where the grains become more distinct. The microstructure changes when the additional Li excess reaches 10%. The pores become larger and even start to separate the grains. At 20% Li excess the grains are clearly separated and large pores are visible, leading to open porosity in the sample. During sintering of the sample, the grain growth can be rather rapid, entrapping gas located in between the particles after pressing or volatilization of excess LiOH, both leading to the observed closed porosity inside the rather large grains. Based on the microstructural features, mechanical stability as well as electrochemical performance are expected to be significantly worse for the samples with significant Li excess. The good sintering behavior of samples containing small amounts of excess Li (0–5%) is due to an earlier start of the formation of the targeted cubic phase as the correct concentration of lithium for incorporation of Ga into the LLZO crystal structure is reached quicker.

This conclusion is underlined by the XRD patterns in the ESI (Fig. SI1†) showing that in case of 0% Li excess only a short dwell time of 1 h is required to obtain the desired cubic phase. Nevertheless, all samples in the back scattered electron images (BSE) show secondary phases that are mainly located between grains or as inclusions in the bulk material (Fig. 6).

In Fig. 7 these additional phases located between the grains are highlighted by different material contrast and the corresponding EDX point analyses. The spectrum at position 1 was taken within a grain, and reflects LLZO:Ga with expected chemical composition in dark gray (note that Li is not detectable in EDX spectra). The brighter region (position 2) is strongly depleted in Zr, while La and Ga contents are enriched, resulting

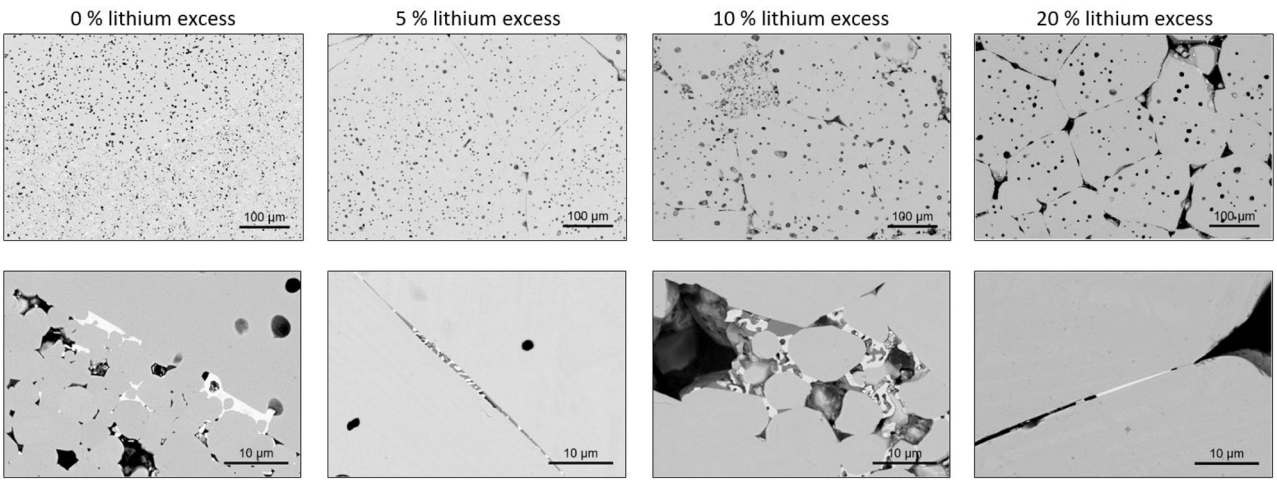

Fig. 6 BSE images of sintered pellets (1175 °C, 5 h) for different Li excess.

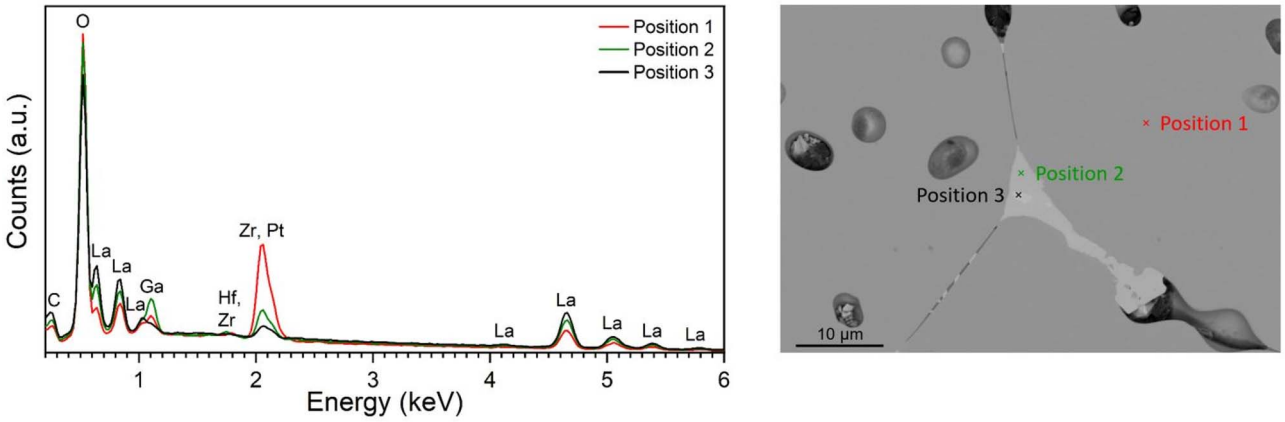

Fig. 7 BSE SEM image of LLZO:Ga without addition of Li (0% Li excess) sintered at 1175 °C for 5 h and corresponding EDX point analyses.

in a higher average atomic number. This indicates that a La- and Ga-rich phase is present between the grains. In the brightest spot (position 3), the La content is even higher than in the surrounding phase (position 2) with even further reduced Zr content and almost no Ga is detected. However, the total amount of these phases is low and therefore below the XRD detection limit and not visible in XRD patterns (Fig. 5). From these results, it is obvious that secondary phases form predominantly between grains (possibly even at triple points of the grains) and that they are independent of Li excess.

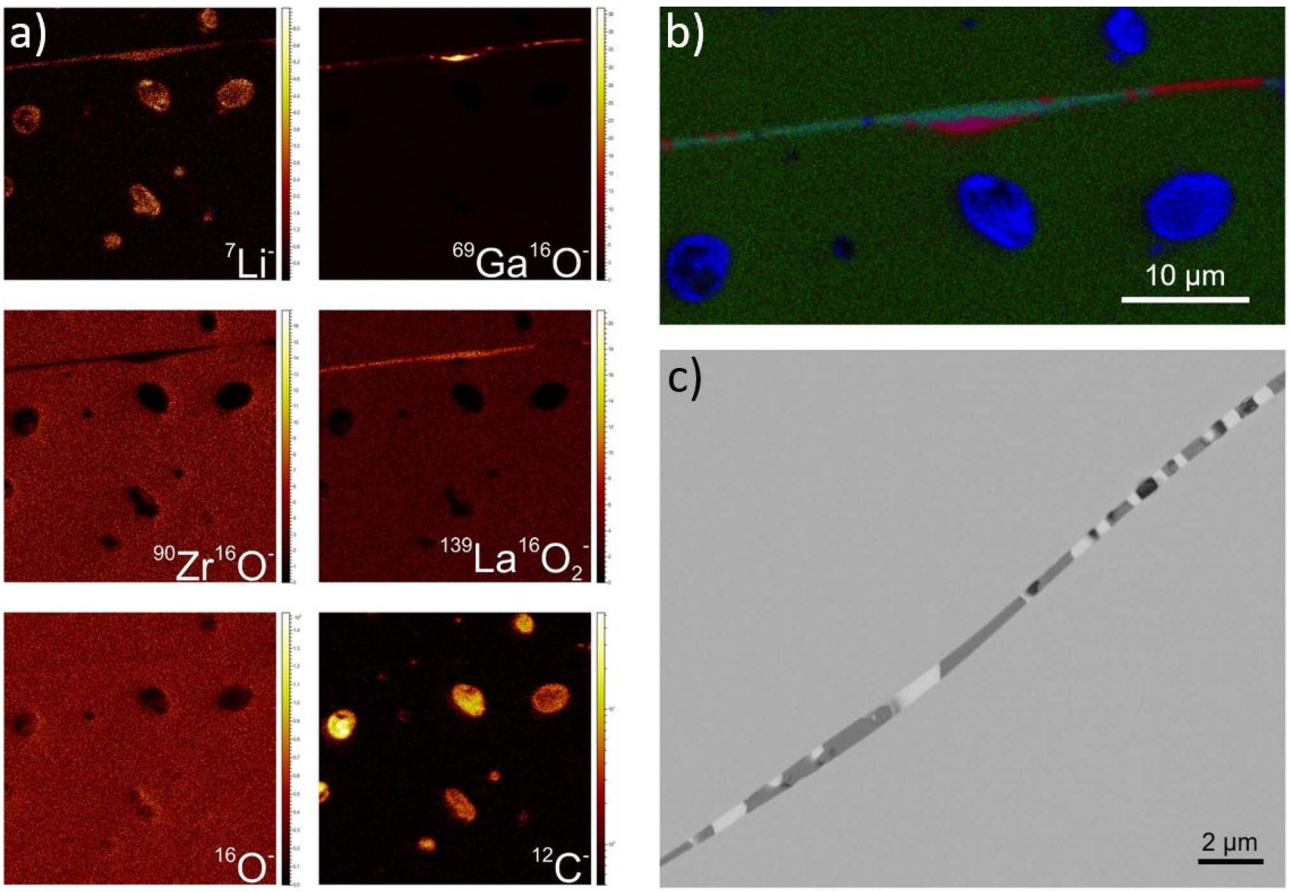

Fig. 8 (a) ToF-SIMS secondary ion images at interphase of negative species present in LLZO:Ga with 0% Li excess as well as C contamination from the reaction with atmospheric CO_2. Image scale: 50 μm × 50 μm (b) RGB overlay of negative secondary ion images representing different phases between grains of LLZO:Ga with 0% Li excess. $^{7}Li^{-}$: blue, $^{69}Ga^{16}O^{-}$: red, $^{139}La^{16}O_2^{-}$: green (c) SEM image of different phases located between grains.

To elucidate the chemical composition of formed phases, high resolution ToF-SIMS analysis, which also enables the detection of Li, was performed on a 0% Li excess sample (Fig. 8a). Carbon, most likely Li_2CO_3, is visible in the pores. The carbon contamination could be from atmospheric CO_2, since cutting, polishing and sample transfer to the SIMS machine took place in air. Higher intensities of $^{7}Li^{-}$, $^{69}Ga^{16}O^{-}$ and $^{139}La^{16}O_2^{-}$ are found between grains, as well as a depletion of $^{90}Zr^{16}O^{-}$. Fig. 8b shows the RGB-overlay of $^{7}Li^{-}$, $^{139}La^{16}O_2^{-}$ and $^{69}Ga^{16}O^{-}$ species. Three distinct phases are observed between the grains: a mainly Ga-containing phase with small amounts of Li, a Li- and Ga-containing phase, and a region where Li, La and Ga are present. This agrees well with the SEM and EDX results, which also indicate an enrichment of Ga and La in the interphases between grains (Fig. 7 and 8c). ToF-SIMS additionally shows an increased intensity of $^{7}Li^{-}$ in this region, which cannot be detected in EDX analyses. In all cases, the oxygen ion image does not show significant differences in the analyzed area. Therefore, it can be assumed that all secondary phases are oxides. Furthermore, these secondary phases must have formed during the sintering process and not due to contamination, since C is not visible between the grains (Fig. 8a). This suggests that Ga acts as a sintering agent and promotes the growth of large grains, but forms separate phases between the grains, which also contain Li, La and O. This observation points to the fact that Ga has a limited solubility in the LLZO phase, and that the solubility limit must be exceeded in the investigated samples. A better electrochemical performance might therefore be achieved with lower Ga-content.

Finally, the electrochemical performance of the best conducting sample LLZO:Ga (5 h, 0% Li excess) is analyzed in detail. A closer look at the impedance spectra measured at different temperatures shows that two different fitting models are required. Low temperature measurements from −40 °C to −10 °C show three semicircles and a low frequency capacitive tail in the Nyquist plot, which can be fitted with an equivalent circuit consisting of a resistor *R*, three *R*-CPE elements and one final CPE-element (Fig. 9a). The resistor *R* is used to describe the resistance above the measurements frequency range and most likely belongs to a bulk phase. At higher temperature (0 to 60 °C) a distinction between bulk phases is no longer possible and the resistor *R* describes the sum of both bulk contributions (Fig. 9b).

To assign the *R*-CPE elements to their corresponding physical counterparts, the effective capacitance *C* was calculated from the fitted resistance *R*, CPE-coefficient *Q*, and exponential parameter α (eqn (1), Table 5).[29,30] α describes the inhomogeneity of the system. For example, a rough or porous surface can cause a double-layer capacitance to appear as a constant phase element with an α value between 0.9 and 1. The case $\alpha = 1$ describes an ideal capacitor, while the case $\alpha = 0$ describes a pure resistor. For the aforementioned capacitance calculation,

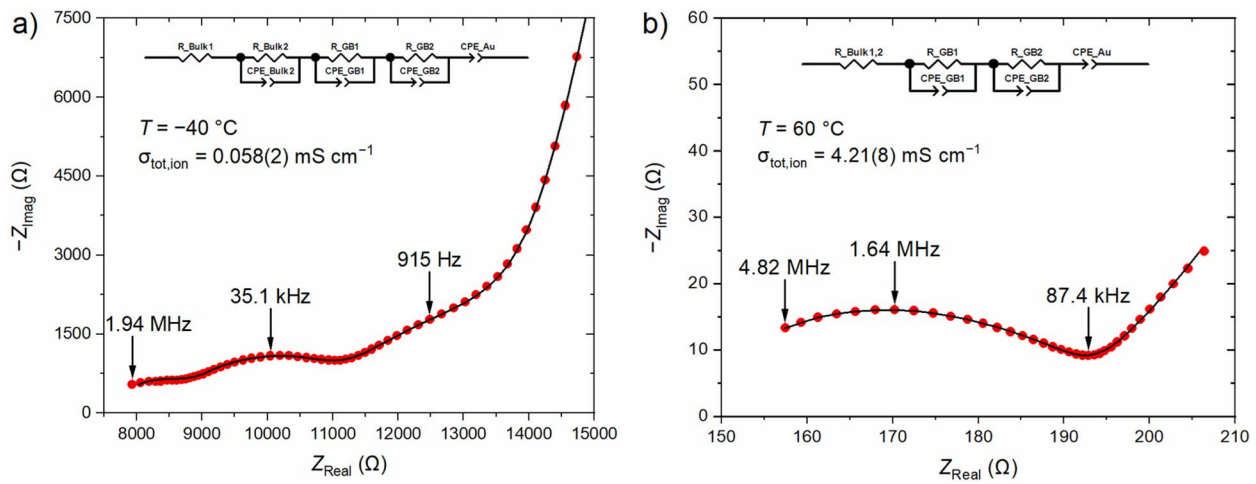

Fig. 9 EIS spectra of LLZO:Ga (5 h, 0% Li excess) measured at (a) −40 °C and (b) +60 °C. Measured data is depicted in red, fitted data in black.

Table 5 EIS results at different temperatures of a 0% Li excess sample sintered for 5 h at 1175 °C

Parameter	−40 °C	0 °C	25 °C	60 °C
R_{Bulk1} (Ω)	7635(15)	735(3)	427(2)	146(1)
R_{Bulk2} (Ω)	1109(21)			
C_{Bulk2} (F)	$1.21(5) \times 10^{-10}$			
R_{GB1} (Ω)	2475(86)	236(7)	135(3)	38.8 (12)
C_{GB} (F)	$1.8(8) \times 10^{-9}$	$1.4(9) \times 10^{-9}$	$1.5(5) \times 10^{-9}$	$1.8(7) \times 10^{-9}$
R_{GB2} (Ω)	2728(167)	66(5)	27.5(16)	6.6(8)
C_{GB2} (F)	$7.6(35) \times 10^{-8}$	$8.3(10) \times 10^{-8}$	$9.4(11) \times 10^{-8}$	$5.8(11) \times 10^{-8}$
$\sigma_{tot,ion}$ (mS cm^{-1})	0.058(2)	0.78(2)	1.37(2)	4.21(8)

α should be at least 0.75 and therefore we constrained all α values to the range of $0.75 < \alpha < 1$. Due to the low contribution of Bulk1 at low temperature ($T < 0$ °C) and GB2 at higher temperature (0 °C $\leq T$), their α values were fixed at 0.9 during the EIS fit. The low-frequency tail is a clear sign of ion-blocking electrodes, typical for gold electrodes, and can be described, for example, by a CPE-element, as previously reported.[4,9]

$$C = \frac{(Q \times R)^{\frac{1}{\alpha}}}{R} \quad (1)$$

The capacitances fit quite well to the reported values for bulk material (10^{-10}–10^{-12} F) and grain boundaries (GB, 10^{-7}–10^{-9} F) in an ion conductor.[31] The total ionic conductivity ($\sigma_{tot,ion}$) was calculated from the total resistance (R_{tot}, the sum of all bulk and GB resistances) of both phases, and pellet geometry (height h and area A) (eqn (2)).

$$\sigma_{tot} = \frac{h}{A \times R_{tot}} \quad (2)$$

Activation energies (E_a) of lithium ion conductivity in LLZO are determined by the Arrhenius equation (eqn (3)).

$$\sigma T \sim \exp\left(\frac{-E_a}{R_g T}\right) \quad (3)$$

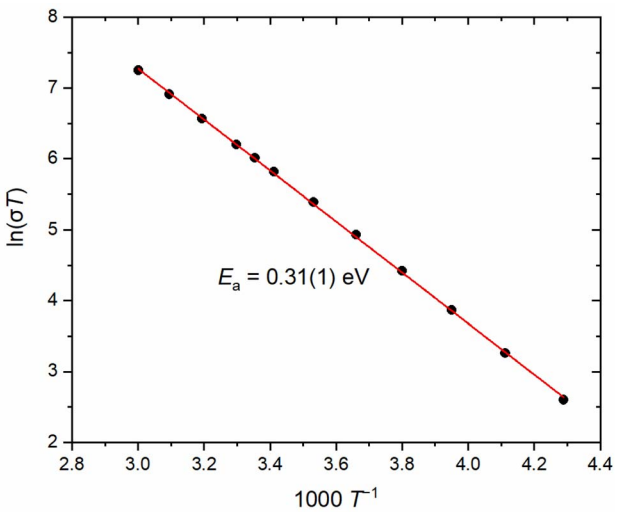

Fig. 10 Arrhenius plot of LLZO:Ga (5 h, 1175 °C 0% Li excess). The determined activation energy is 0.31(1) eV.

Table 6 Total ionic conductivity in mS cm^{-1} of LLZO at 25 °C depending on dwell time and used lithium excess

		Dwell time			
		1 h	5 h	10 h	20 h
Lithium excess	0%	0.42(1)	1.37(2)	0.28(1)	0.45(8)
	5%	0.04(1)	0.18(1)	0.13(1)	0.19(1)
	10%	0.05(1)	0.08(1)	0.11(1)	0.13(2)
	20%	0.01(1)	0.02(1)	0.05(1)	0.04(1)

Table 7 Activation energies in eV of lithium ion conduction in LLZO depending on dwell time and lithium excess

		Dwell time			
		1 h	5 h	10 h	20 h
Lithium excess	0%	0.47(1)	0.31(1)	0.34(1)	0.35(1)
	5%	0.38(1)	0.35(1)	0.38(1)	0.36(1)
	10%	0.38(1)	0.37(1)	0.37(1)	0.38(1)
	20%	0.42(1)	0.39(1)	0.38(1)	0.38(1)

Table 8 Comparison of processing parameters, conductivity and activation energies of the studied nominal composition $Li_{6.4}Ga_{0.2}La_3Zr_2O_{12}$

Li excess (%)	Sinter conditions	Rel. density (%)	$\sigma_{tot,ion}$ (mS cm^{-1}) at T = 25 °C	E_a (eV)
0	1 h, 1175 °C	91.2	0.42(1)	0.47(1)
0	5 h, 1175 °C	97.3	1.37(2)	0.31(1)
0	10 h, 1175 °C	92.7	0.28(1)	0.34(1)
0	20 h, 1175 °C	91.1	0.45(8)	0.35(1)
5	1 h, 1175 °C	94.5	0.04(1)	0.38(1)
5	5 h, 1175 °C	94.6	0.18(1)	0.35(1)
5	10 h, 1175 °C	92.7	0.13(1)	0.38(1)
5	20 h, 1175 °C	93.4	0.19(1)	0.36(1)
10	1 h, 1175 °C	93.5	0.05(1)	0.38(1)
10	5 h, 1175 °C	93.5	0.08(1)	0.37(1)
10	10 h, 1175 °C	92.0	0.11(1)	0.37(1)
10	20 h, 1175 °C	91.8	0.13(2)	0.38(1)
20	1 h, 1175 °C	91.2	0.01(1)	0.42(1)
20	5 h, 1175 °C	91.8	0.02(1)	0.39(1)
20	10 h, 1175 °C	91.5	0.05(1)	0.38(1)
20	20 h, 1175 °C	90.1	0.04(1)	0.38(1)

R_g describes the universal gas constant and T the absolute temperature. The Arrhenius plot ($\ln(\sigma T)$ *vs.* $1000T^{-1}$) is shown in Fig. 10 resulting in E_a = 0.31(1) eV for LLZO:Ga (5 h, 0% Li excess). While the determined conductivities of all samples at 25 °C can be found in Table 6, activation energies of these samples are summarized in Table 7. The EIS spectra of all temperatures and their corresponding fit results can be found in the ESI (Fig. SI2 and Table SI2†).

Unfortunately, the preparation of symmetrical cells to test for the critical current density and cycle stability is not possible at such Ga levels. Melting Li metal on top of the LLZO:Ga separators resulted in decomposition along grain boundaries and the samples falling apart. This behavior was already reported in literature.[8] The additional Li–La–Ga phases first reported in this study may be the cause of decomposition.

Conclusions

Table 8 summarizes all processing and electrochemical performance parameters of this study. The systematic determination of these values allows a detailed analysis of the effects of the process parameters on the electrochemical performance. Contrary to general assumption, this study shows that Li excess can have a significant impact on electrochemical performance,

i.e., lower ionic conductivity and higher activation barriers. From a mechanistic point of view, two interrelated phenomena were found. First, with increasing Li excess, a secondary tetragonal phase with poorer ionic conductivity is formed (Fig. 2 and SI1†). To remove this phase, long dwell times are necessary to evaporate additional Li and form the desired cubic phase. Obviously, it is undesirable in industrial applications because the consumption of precursors and energy has a negative impact on the manufacturing costs. Second, the excess of Li also leads to a different microstructure (Fig. 5). Without additional Li, a homogeneous pellet is obtained, while with higher amounts of excess lithium, the grains become increasingly separated by pores and voids. This has a negative effect on the mechanical properties and electrochemical performance of the final ceramic electrolyte, and thus on the industrial viability of the material.

Finally, the observed Li–La–Ga phases between grains can also affect the electrochemical performance. They can be found in all samples regardless of Li excess and might originate from a solubility limit of Ga in the cubic phase. Atomic level investigations are needed to fully elucidate this phenomenon, but the results of this study suggest that a slight reduction of Ga during synthesis could reduce the secondary phase formation.

In summary, the Li excess and dwell time are the key factors that need to be precisely controlled to achieve good microstructure and electrochemical performance of LLZO:Ga. The peak performance that justifies the use of Ga as substituent is only achievable within a small processing window. While some excess of Li can be beneficial, high amounts of excess Li can actually prevent good electrochemical performance or at least require unprofitably long heating and processing times. In this study, it has been shown for the first time that having no excess Li is most beneficial for efficient synthesis and processing of LLZO:Ga (unlike LLZO, *e.g.*, substitution with Al, Ta or Nb). The underlying mechanism is an intricate interplay between the phase equilibria of different phases (tetragonal, cubic, Li–La–Ga), which (in small amounts) exhibit good conductivity and/or serve as sintering aids, but in large amounts are detrimental for electrochemical performance.

Therefore, robust and reproducible processing that takes advantage of these different properties and substitution within the LLZO family can make industrial processing viable and economic.

Author contributions

Conceptualization, G. H., M. M. and M. F.; funding acquisition, O. G. and M. F.; investigation, C. S., G. H., M. M., and C. R.; project administration, D. F.-R. and M. F.; resources, M. M. and G. H.; supervision, M. F.; writing—original draft, C. S., G. H. and M. M.; writing—review & editing, C. S., G. H., M. M., C. R., O. G., D. F.-R., and M. F. All authors have read and agreed to the published version of the manuscript.

Conflicts of interest

The authors do not have any conflicts of interest to declare.

Acknowledgements

The authors gratefully acknowledge the financial support by the German Federal Ministry of Education and Research (BMBF) as part of the projects "FestBatt2-Oxide" (FKZ: 13XP0434A), "FestBatt2-Production" (FKZ: 13XP0432B) and "Meet Hi-EnD III" (FKZ: 13XP0258B) as well as the "Deutsche Forschungsgemeinschaft" (DFG) within the project "E-TIP" (FKZ: 429409150). The authors thank D. Sebold (IEK-1) for contributions to the SEM investigations, the Central Institute of Analytics (ZEA-3) for the ICP-OES measurements and providing access to the ToF-SIMS machine.

Notes and references

1 H. Buschmann, J. Dölle, S. Berendts, A. Kuhn, P. Bottke, M. Wilkening, P. Heitjans, A. Senyshyn, H. Ehrenberg, A. Lotnyk, V. Duppel, L. Kienle and J. Janek, *Phys. Chem. Chem. Phys.*, 2011, **13**, 19378–19392.
2 R. Murugan, V. Thangadurai and W. Weppner, *Angew. Chem., Int. Ed.*, 2007, **46**, 7778–7781.
3 C.-L. Tsai, E. Dashjav, E.-M. Hammer, M. Finsterbusch, F. Tietz, S. Uhlenbruck and H. P. Buchkremer, *J. Electroceram.*, 2015, **35**, 25–32.
4 M. Mann, M. Küpers, G. Häuschen, M. Finsterbusch, D. Fattakhova-Rohlfing and O. Guillon, *Ionics*, 2021, **28**, 53–62.
5 Y. Li, J.-T. Han, C.-A. Wang, H. Xie and J. B. Goodenough, *J. Mater. Chem.*, 2012, **22**, 15357–15361.
6 J. F. Wu, W. K. Pang, V. K. Peterson, L. Wei and X. Guo, *ACS Appl. Mater. Interfaces*, 2017, **9**, 12461–12468.
7 R. Wagner, G. J. Redhammer, D. Rettenwander, A. Senyshyn, W. Schmidt, M. Wilkening and G. Amthauer, *Chem. Mater.*, 2016, **28**, 1861–1871.
8 C. L. Tsai, N. T. Thuy Tran, R. Schierholz, Z. Liu, A. Windmüller, C.-a. Lin, Q. Xu, X. Lu, S. Yu, H. Tempel, H. Kungl, S.-k. Lin and R.-A. Eichel, *J. Mater. Chem. A*, 2022, **10**, 10998–11009.
9 D. Rettenwander, G. Redhammer, F. Preishuber-Pflugl, L. Cheng, L. Miara, R. Wagner, A. Welzl, E. Suard, M. M. Doeff, M. Wilkening, J. Fleig and G. Amthauer, *Chem. Mater.*, 2016, **28**, 2384–2392.
10 C. Bernuy-Lopez, W. Manalastas, J. M. Lopez del Amo, A. Aguadero, F. Aguesse and J. A. Kilner, *Chem. Mater.*, 2014, **26**, 3610–3617.
11 X. Xiang, F. Chen, Q. Shen, L. Zhang and C. Chen, *Mater. Res. Express*, 2019, **6**, 085546.
12 S. Kim, J. S. Kim, L. Miara, Y. Wang, S. K. Jung, S. Y. Park, Z. Song, H. Kim, M. Badding, J. Chang, V. Roev, G. Yoon, R. Kim, J. H. Kim, K. Yoon, D. Im and K. Kang, *Nat. Commun.*, 2022, **13**, 1883.
13 M. Finsterbusch, T. Danner, C.-L. Tsai, S. Uhlenbruck, A. Latz and O. Guillon, *ACS Appl. Mater. Interfaces*, 2018, **10**, 22329–22339.
14 L. Robben, E. Merzlyakova, P. Heitjans and T. M. Gesing, *Acta Crystallogr., Sect. E: Crystallogr. Commun.*, 2016, **72**, 287–289.

15 K. Kataoka and J. Akimoto, *Solid State Ionics*, 2020, **349**, 115312.
16 D. O. Shin, K. Oh, K. M. Kim, K. Y. Park, B. Lee, Y. G. Lee and K. Kang, *Sci. Rep.*, 2015, **5**, 18053.
17 M. Mann, M. Küpers, G. Häuschen, M. Finsterbusch, D. Fattakhova-Rohlfing and O. Guillon, *Materials*, 2021, **14**, 6809.
18 N. Hamao and K. Hamamoto, *J. Asian Ceram. Soc.*, 2022, **10**, 1–8.
19 S. Qin, X. Zhu, Y. Jiang, M. Ling, Z. Hu and J. Zhu, *Appl. Phys. Lett.*, 2018, **112**, 113901.
20 W. Lan, H. Fan, V. W.-h. Lau, J. Zhang, J. Zhang, R. Zhao and H. Chen, *Sustainable Energy Fuels*, 2020, **4**, 1812–1821.
21 J. F. Wu, E. Y. Chen, Y. Yu, L. Liu, Y. Wu, W. K. Pang, V. K. Peterson and X. Guo, *ACS Appl. Mater. Interfaces*, 2017, **9**, 1542–1552.
22 H. El Shinawi and J. Janek, *J. Power Sources*, 2013, **225**, 13–19.
23 J. F. Wu, B. W. Pu, D. Wang, S. Q. Shi, N. Zhao, X. Guo and X. Guo, *ACS Appl. Mater. Interfaces*, 2019, **11**, 898–905.
24 J. Rodríguez-Carvajal, *Phys. B*, 1993, **192**, 55–69.
25 J. F. Bérar and P. Lelann, *J. Appl. Crystallogr.*, 1991, **24**, 1–5.
26 R. Ye, C.-L. Tsai, M. Ihrig, S. Sevinc, M. Rosen, E. Dashjav, Y. J. Sohn, E. Figgemeier and M. Finsterbusch, *Green Chem.*, 2020, **22**, 4952–4961.
27 R. Kun, F. Langer, M. Delle Piane, S. Ohno, W. G. Zeier, M. Gockeln, L. Colombi Ciacchi, M. Busse and I. Fekete, *ACS Appl. Mater. Interfaces*, 2018, **10**, 37188–37197.
28 R. Ye, M. Ihrig, N. Imanishi, M. Finsterbusch and E. Figgemeier, *ChemSusChem*, 2021, **14**, 4397–4407.
29 M. E. Orazem, I. Frateur, B. Tribollet, V. Vivier, S. Marcelin, N. Pébère, A. L. Bunge, E. A. White, D. P. Riemer and M. Musiani, *J. Electrochem. Soc.*, 2013, **160**, C215–C225.
30 C. H. Hsu and F. Mansfeld, *Corrosion*, 2001, **57**, 747–748.
31 J. T. S. Irvine, D. C. Sinclair and A. R. West, *Adv. Mater.*, 1990, **2**, 132–138.